

# Spintronic Neuromorphic Hardware Using Domain Wall Based Neurons and Quantized Synapses

Sakshi Kiran Bandekar,<sup>1</sup> Arnab Ganguly,<sup>2</sup> Debanjan Polley\*,<sup>3</sup> and Debasis Das\*<sup>1</sup>

<sup>1</sup>*Department of Electrical and Electronics Engineering,*

*Birla Institute of Technology and Science, Pilani, K K Birla Goa Campus, Goa 403726, India*

<sup>2</sup>*Department of Physics and Nanotechnology, SRM Institute of Science and Technology, Kattankulathur, Tamil Nadu 603203, India*

<sup>3</sup>*Department of Physics, Birla Institute of Technology and Science, Pilani, Jawahar Nagar, Kapra Mandal, Medchal District, Telangana 500078, India\**

In this work, we simulate the functionality of artificial neuron and synapse using spin-orbit torque-based spintronic devices and implemented a fully connected artificial neural network (ANN). These neuro-synaptic devices are emulated using transverse domain wall dynamics in a rectangular magnetic nanotrack comprised of heavy metal/ferromagnet (HM/FM) heterostructures. The ReLU activation function of the neuron has been mimicked using the domain wall motion induced by a 3 ns current pulse. The synapse has been modelled using current-induced domain wall (DW) dynamics through a corrugated HM/FM nanotrack under the influence of a 10 ns current pulse with varying current density. The semicircular corrugations are in the form of notches, which are symmetrically located on both sides of the nanotrack. By applying 10 ns current pulses of varying densities, we achieve controlled DW pinning, revealing a step-like motion caused by temporary pauses at each pinning center. The electrical conductance of the pinned DW across various pinning points, act as stable synaptic weights for our ANN. Furthermore, we observe a threshold-dependent delay effect where each depinning event is influenced by previous ones, successfully mimicking synaptic memory and adaptability in neuromorphic systems. The fully connected ANN has been modeled using the conventional float32 synaptic weights for the MNIST and Fashion MNIST datasets with an accuracy of  $\sim 97\%$  and  $\sim 86\%$  respectively, which serves as a test bed of our neuromorphic simulations. With the aim of implementing a sparse and low memory footprint ANN, we quantize the trained synaptic weights into discrete quantized level and tested the network, which demonstrate an accuracy of  $\sim 95\%$  and  $\sim 62\%$ , for the MNIST and Fashion-MNIST dataset, respectively. Although direct quantization impacted performance, fine-tuning the network fully restored accuracies to near-baseline levels. These findings highlight the potential of engineered DW pinning-depinning dynamics for scalable, adaptive, and hardware-efficient neuromorphic computing.

## I. INTRODUCTION

The algorithm of artificial intelligence (AI) dates back to the decade of 1940's led by the pioneering work of Warren McCulloch and Walter Pitts[1], Donald O. Hebb[2]. The usage of AI has exploded exponentially since the last decade, due to the development of semiconductor fabrication technology and the various hardware accelerators[3]. Scientists are using AI in almost every field spanning from material discovery[4], band structure calculation[5, 6], drug discovery[7, 8], computer vision[9, 10], medical imaging[11, 12], *etc.* Inspired by the highly interconnected, parallel processing of biological neurons and the nervous system's ability to learn and adapt, artificial neural networks (ANNs) were designed as computational systems that mimic this organization by adjusting weighted connections to analyze complex information and map inputs to outputs. However, implementing a massive parallelism on traditional hardware is hindered by the von Neumann bottleneck, which requires constant, energy-intensive data transfer. Therefore, researchers implement ANNs using emerging non-volatile memory (eNVM) devices such as resistive random access memory [13–15], phase change memory [16–19], spintronics[20–23] devices. Among these various eNVM devices, spintronics-based devices stand out as a superior choice owing to ultrafast dynamics[24–26], low power consumption[27, 28], high endurance[29]. Fundamental spintronic device such as magnetic tunnel junction (MTJ) offers two distinct stable resistance states[30, 31] based on the magnetoresistive[32] phenomenon. Such devices

with binary states have proven to be an excellent choice for implementing digital memory [33–35]; however, neuromorphic computing requires memory elements capable of mimicking the inherently analog function of the biological brain. On the other hand, a magnetic domain wall (DW) is a magnetic texture that separates magnetic domains of opposite magnetization, and its precise manipulation using electric currents or magnetic fields makes DWs promising candidates for high-density memory, logic operations, and adaptive computational systems. Such magnetic DW-based devices could mimic the analog nature, by utilizing the position of the DW to encode multiple intermediate, resistance states, which directly implement the continuously adjustable synaptic weights.

Neural network could be trained online, where the training involves direct modification of the synaptic weights within the non-volatile memory hardware itself, a process that is often time-consuming due to the low speed of iterative write/erase cycles and costly due to the high energy consumption per training epoch. Alternatively, the network can undergo offline training (or ex-situ training), where the training is performed using high-performance computing resources, such as GPUs or conventional CPUs, utilizing frameworks like PyTorch. After completion of the training, the final, optimized synaptic weights are transferred to and fixed within the non-volatile memory hardware for the inference stage. This approach significantly reduces the latency and energy costs associated with the long training process on the resource-constrained eNVM hardware. Thus, stability of the synaptic weight is of utmost importance when an ANN is used for inference on edge devices with

an expectation of longer lifetime. However, due to stray field or demagnetization fields the position of the DW could be displaced[36], which would hinder the stability of the pretrained synaptic, and eventually causing a lower inference accuracy. Therefore, the necessity of having a well-controlled synapse that exhibits high stability for holding synaptic weights becomes the central focus for enabling reliable, long-term inference on power-constrained edge devices using DW-based neuromorphic hardware. With the ongoing development of spintronics-based fabrication technology, we can surely hope for implementing a complete DW-based neuro-synaptic hardware. However, at this early stage, this requires a well-defined model for the DW-based neuron and synapse to accurately capture their behavior, followed by a thorough evaluation of the performance of the ANN built using these model-defined components. With this aim in mind, we have designed a magnetic DW-based neuron and synapse device on thin HM/FM nanotrack and performed micromagnetic simulation to obtain their corresponding functionalities. We propose a design for the DW-based neuron that mimic the functionality of a simple and hardware friendly ReLU activation function to bypass the known issues of dead-neuron problem that occurs in the sigmoid activation function[37]. We have added well-defined pinning sites across the nanotrack to ensure the stability of the synaptic weights against any unwanted displacement due to stray magnetic field. This gives rise to quantized conductance states which is used to design a fully connected quantized neural network (QNN). First, a software-based training is performed using PyTorch to train a fully connected neural network, with the custom ReLU-like activation function obtained from our proposed neuron. Then, the trained float32 (FP32) weights are quantized according to the discrete conductance states obtained from the proposed synapse device, and the network is trained again for fine-tuning those quantized weights. Network with the fine-tuned weights shows the inference accuracy very similar to the network with FP32 weight counterpart.

## II. MICROMAGNETIC SIMULATION DETAILS & DEVICE STRUCTURE

In this section, we describe the device structure for our proposed artificial neuron and synapse and the details of the micromagnetic framework that has been used for the simulation. We simulated both neuron and synapse functionalities by leveraging the temporal dynamics of magnetization (*i.e.* the DW motion) within a HM/FM nanotrack. The micromagnetic simulation has been performed by numerically solving the Landau-Lifshitz-Gilbert-Slonczewski (LLGS) equation[38] as given below

$$\frac{d\mathbf{m}}{dt} = \gamma(\mathbf{m} \times \mathbf{H}_{eff}) + \alpha \left( \mathbf{m} \times \frac{d\mathbf{m}}{dt} \right) + \gamma\beta\epsilon(\mathbf{m} \times \mathbf{m}_p \times \mathbf{m}) - \gamma\beta\epsilon'(\mathbf{m} \times \mathbf{m}_p). \quad (1)$$

where,  $\mathbf{m}$  is the magnetization unit vector,  $\mathbf{H}_{eff}$  is the effective magnetic field consisting of uniaxial anisotropy field, demagnetization field, external magnetic field and the field due to Dzyaloshinskii-Moriya interaction (DMI).  $\gamma$  is the gyromagnetic ratio,  $\alpha$  is the damping factor,

TABLE I. Device simulation parameters

Parameter	Symbol	Value
Gyromagnetic ratio	$\gamma$	$2.211 \times 10^5$ m/(A·s)
Reduced Planck's Constant	$\hbar$	$1.054 \times 10^{-34}$ J·s
Free space permeability	$\mu_0$	$4\pi \times 10^{-7}$ N/A <sup>2</sup>
Electronic charge	$e$	$1.602 \times 10^{-19}$ C
FM free layer thickness	$t_{FM}$	2 nm
Polarization	$P$	0.4
Saturation magnetization	$M_S$	$1.1 \times 10^6$ A/m
Exchange stiffness constant	$A_{ex}$	$2.0 \times 10^{-11}$ J/m
DMI constant	$D$	1-2 mJ/m <sup>2</sup>
Anisotropy constant	$K_u$	$10^6$ J/m <sup>3</sup>

$\mathbf{m}_p$  is the spin polarization direction of the spin current in the ferromagnet (FM) layer. Apart from these,  $\beta = \hbar P J / (2\mu_0 e t_{FM} M_S)$ , and  $\epsilon = \frac{P^2 \Lambda}{(\Lambda^2 + 1) + (\Lambda^2 - 1)(\mathbf{m} \cdot \mathbf{m}_p)}$ . Details of the parameters are given in Table I. The magnetization dynamics is simulated in open-source object-oriented micromagnetic framework (OOMMF)[39] with DMI extension module[40] and UBERMAG[41]. Fig. 1(a) illustrates a 3d schematic of the proposed artificial neuron, which integrates a HM layer with a FM layer, referred to as free layer (FL). The dimension of both layers are considered to be 512 nm×64 nm×2 nm. We replicate the functionality of the ReLU activation function using our proposed magnetic DW-based artificial neuron device. The FL contains two magnetic domains: one with magnetization pointing in the  $+z$ -direction (red region) and the other in the  $-z$ -direction (blue region). A magnetic DW is shown as the white region which separates these two domains, and its position is encoded as the measure of conductance of the device. When an electric current is applied to the heavy-metal (HM) layer along the  $+x$ -direction, the spin-Hall effect generates spin-polarized electrons along  $\pm y$ -direction and accumulate at the top and bottom surface of the HM layer. This spin accumulation leads to a spin current flowing in the  $+z$ -direction, which in turn creates a spin-orbit torque (SOT). The SOT can alter (depending on the amplitude, direction and duration of the current pulse) the local magnetization of the FL, causing the DW to move along the  $+x$ -direction. The position of the DW is being used to measure the conductance of the device, using an MTJ-like detector placed on the FL, spanning from  $x = 128$  nm to 384 nm. As illustrated in Fig. 1(a), the detector comprises an oxide layer and a pinned layer (PL), with its magnetization fixed along the  $-z$ -direction.

The synapse has been modelled using a different HM/FM nanotrack. The FM (and the HM) layers are 1500 nm in length, 150 nm in width and a thickness of 2 nm. However, unlike our neuron model, we have introduced symmetrical notch-type corrugations at regular interval as shown in Fig 1(d) in the nanotrack to manipulate the motion of domain walls. We have varied the number of corrugations (5 and 10 notches) to get different number of synaptic weights for the ANN. The DW position is approximated using the average magnetization of the rectangular nanotrack along its length. The magnetization dynamics have been simulated in the presence of a 10 ns square current pulse along

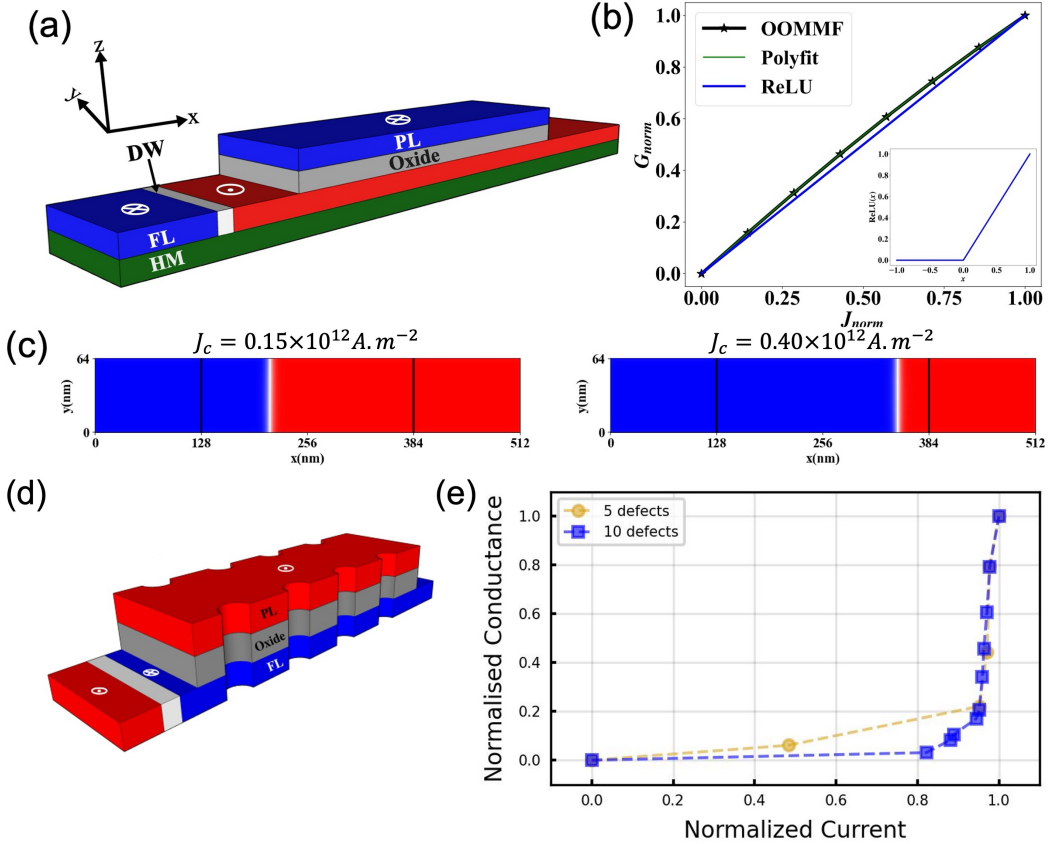


FIG. 1. **Schematic of the proposed spintronic devices to mimic both neuron and synapse.** (a) Schematic 3D figure of the proposed neuron device; (b) Plot of normalized conductance vs. applied current density for the neuron, demonstrating ReLU-like activation function for the positive input. Inset shows the plot of the actual ReLU activation function for both positive as well as negative input values; (c) Two-dimensional color plot for  $m_z$  on the  $x$ - $y$  plane of the  $FL$  for  $J_c = 0.15 \times 10^{12}$  and  $0.40 \times 10^{12}$  A/m<sup>2</sup>; 3D schematic of the proposed synapse device using symmetric (d) notch-type corrugation and (e) Plot of normalized conductance vs. the applied current density for the synapse using different numbers of symmetric notches across the nanotrack

the length ( $x$ -axis) of the nanotrack with varying current density. A DMI energy of 1 mJ/m<sup>2</sup> has been considered to mimic the HM/FM interface and deterministically switch the magnetization via symmetry breaking.

### III. RESULTS AND DISCUSSION

In this section, we discuss the emulation of neuron and synapse functionality using our proposed DW-based devices. As mentioned in Sec. II, the dimension of the FL is 512 nm along length, 64 nm along width, with a thickness of 2 nm, we used a mesh size of 1 nm×1 nm×2 nm in our simulation. Initially, the DW was outside of the detector, *i.e.* towards the left side of the nanotrack, and the detector region of the FL had the magnetic domain whose magnetization was along the  $+z$ -direction (Fig. 1(a)). At this stage, the conductance is minimal due to the opposite magnetization direction of the PL and FL. Conductance across the detector is calculated using the conductance of the MTJ-like structure, which is given by[42]

$$G = G_0 \sum_i \frac{1 + P^2 \cos \theta_i}{1 + P^2} \quad (2)$$

where,  $G_0$  is the conductance when all spins of the FL and PL of the detector are perfectly parallel to each other.  $\theta_i$  is the relative angle between the magnetizations of the  $i$ th cell of FL and the corresponding cell of the PL in the detector. With an increase in current density ( $J$ ), the DW moves along the  $+x$ -direction, and the dominance of the  $-z$  magnetized domain increases in the detector region. We apply the current with different current density values from  $J = 0.1 \times 10^{12}$  to  $.45 \times 10^{12}$  A/m<sup>2</sup> with a step of  $0.05 \times 10^{12}$  A/m<sup>2</sup>, for a span of 3 ns. Fig. 1(b), illustrates the how the normalized conductance ( $G_{norm}$ ) changes with the normalized current density ( $J_{norm}$ ), as shown by the label ‘OOMMF’. Here, both the parameters are normalized using the formula:

$$f_{norm} = \frac{f - f_{min}}{f_{max} - f_{min}} \quad (3)$$

where,  $f$  is the variable we want to normalize,  $f_{max}$  ( $f_{min}$ ) is the maximum (minimum) value of the corresponding variable. The ReLU activation function, is given by  $f(x) = \max(0, x)$ , which basically states that for *negative* values of  $x$ , it remains 0, and for *positive* values, it follows straight line formula of  $y = x$ . The function is shown in the inset of Fig. 1(b). Our device characteristics, *i.e.* the normalized plot of  $G_{norm}$  vs.  $J_{norm}$ , shows a slight deviation from the

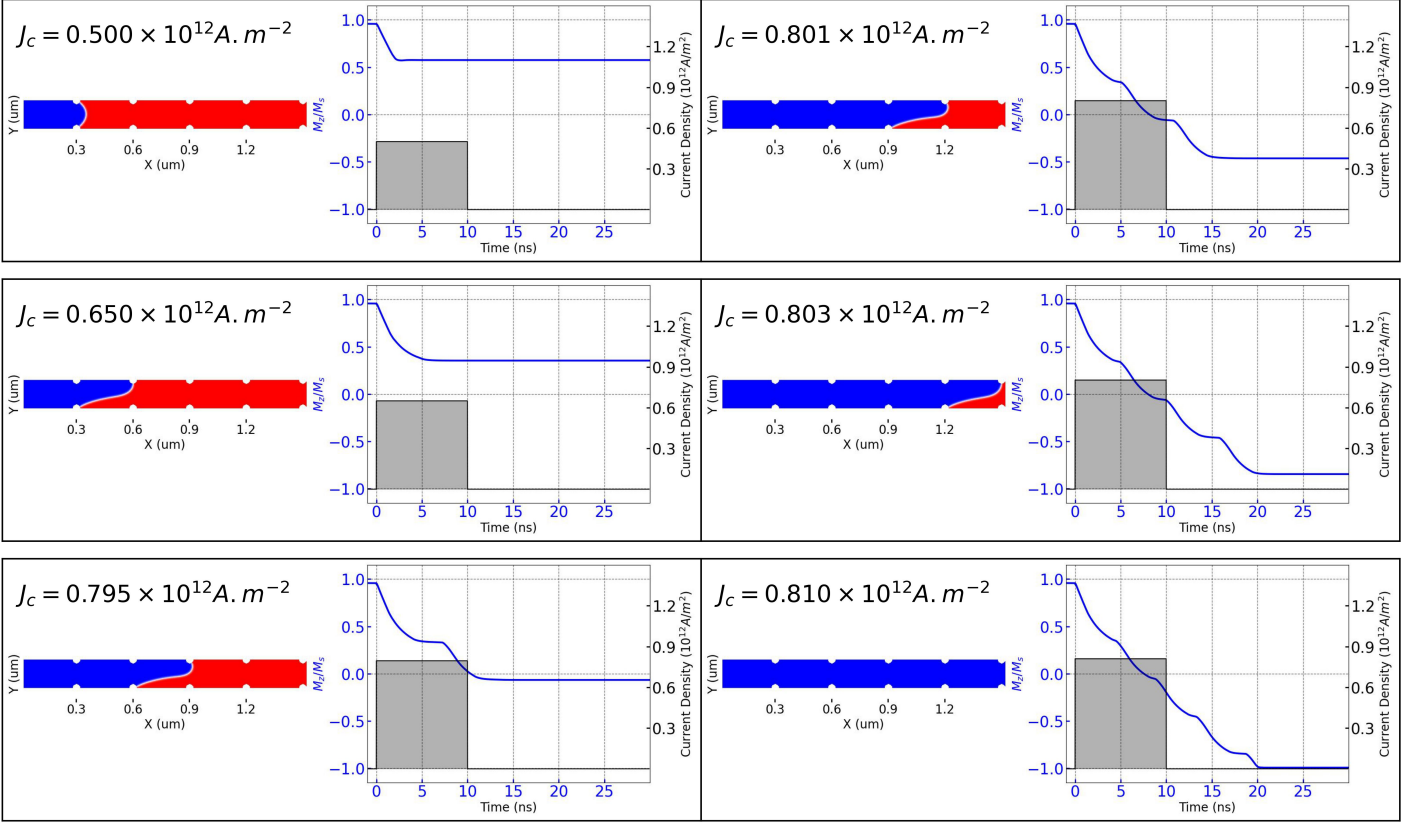


FIG. 2. **Domain wall dynamics through the corrugated magnetic nanotrack containing 5 symmetrical notches.** The magnetization profile within the corrugated magnetic notches as a function of increasing current density of the 10 ns current pulse. The magnetization profile are shown in left and the corresponding time-resolved magnetization dynamics is shown at right at different current densities. The black-shaded region depicts the 10 ns current pulse with increasing current density. The step-like behaviour suggests the pinning of the domain wall at the engineered equidistant notches on the magnetic nanotrack.

ideal ReLU function as shown in the figure. To account for the deviation, we fit our obtained characteristics with a 4<sup>th</sup> order polynomial, as shown by the green line with a label of ‘Polyfit’. The negative part of the characteristics is not shown exclusively in the figure, as the negative current density leads to the motion of the DW towards left side, and for every negative  $J$  values, the conductance remains at its minimum value, which translates to zero value according to Eq.(3). Fig 1(c) shows two-dimensional color plots of the current-induced domain wall motion through the nanotrack for 3-ns square current pulses with current densities  $J = .15 \times 10^{12}$  and  $.40 \times 10^{12}$  A/m<sup>2</sup>. The two black vertical lines represent the region over which the detector is placed. With increasing current density, the DW moves toward right side and the  $-z$  magnetized domain becomes dominant under the detector region, which leads to the increasing conductance as seen in Fig 1(b).

As mentioned in Sec. II, the synapse geometry is larger both in length (1500 nm) and width (150 nm), we have used the mesh size as 3 nm $\times$ 3 nm $\times$ 2 nm for the micromagnetic simulation. Fig. 2 illustrates the magnetization profile of the DW dynamics[43] in a of HM/FL corrugated magnetic nanotrack, due to the application of a 10 ns current pulse with increasing current density. Here, five equally spaced semicircular notches, each with a diameter of 20 nm, acts as the DW manipulation centre. The red (blue) color signifies

$z$ -component of the magnetization of FL pointing up (down) direction. The corresponding time-resolved magnetization dynamics are shown next to the colour profile for each current density where the domain wall gets pinned at the designated pinning sites. The black-shaded region depicts the 10 ns square current pulse for different current densities. A decreasing magnetization value over time indicates that the DW is moving from left to right, with the slope representing the average velocity of the wall. The first notch has been placed at a distance of 300 nm from the left edge of the magnetic nanotrack and the spatial distance between each notches (along the length) are 300 nm. Our simulation shows a current density of  $0.500 \times 10^{12}$  A/m<sup>2</sup> is required for the DW to stabilize at this first notch. Fig. 2(b) shows that it takes  $\sim 2$  ns for the domain wall to move to the first notch, translating a domain wall velocity of  $\sim 150$  m/s. When the current density is increased to  $J = 0.650 \times 10^{12}$  A/m<sup>2</sup>, the DW bypasses the first notch and gets pinned at the second notch at  $x = 600$  nm. Similarly, at  $J = 0.795 \times 10^{12}$  A/m<sup>2</sup>,  $0.801 \times 10^{12}$  A/m<sup>2</sup>, and  $0.803 \times 10^{12}$  A/m<sup>2</sup>, the DW stabilizes at the consecutive notches, located at  $x = 900$  nm,  $1200$  nm, and  $1500$  nm, respectively. Finally, at  $J = 0.810 \times 10^{12}$  A/m<sup>2</sup>, the DW bypasses all notches and traverses the entire nanotrack and it switches the whole magnetization of the nanotrack from  $+z$  to  $-z$  direction. The full switching takes  $\sim 20$  ns using

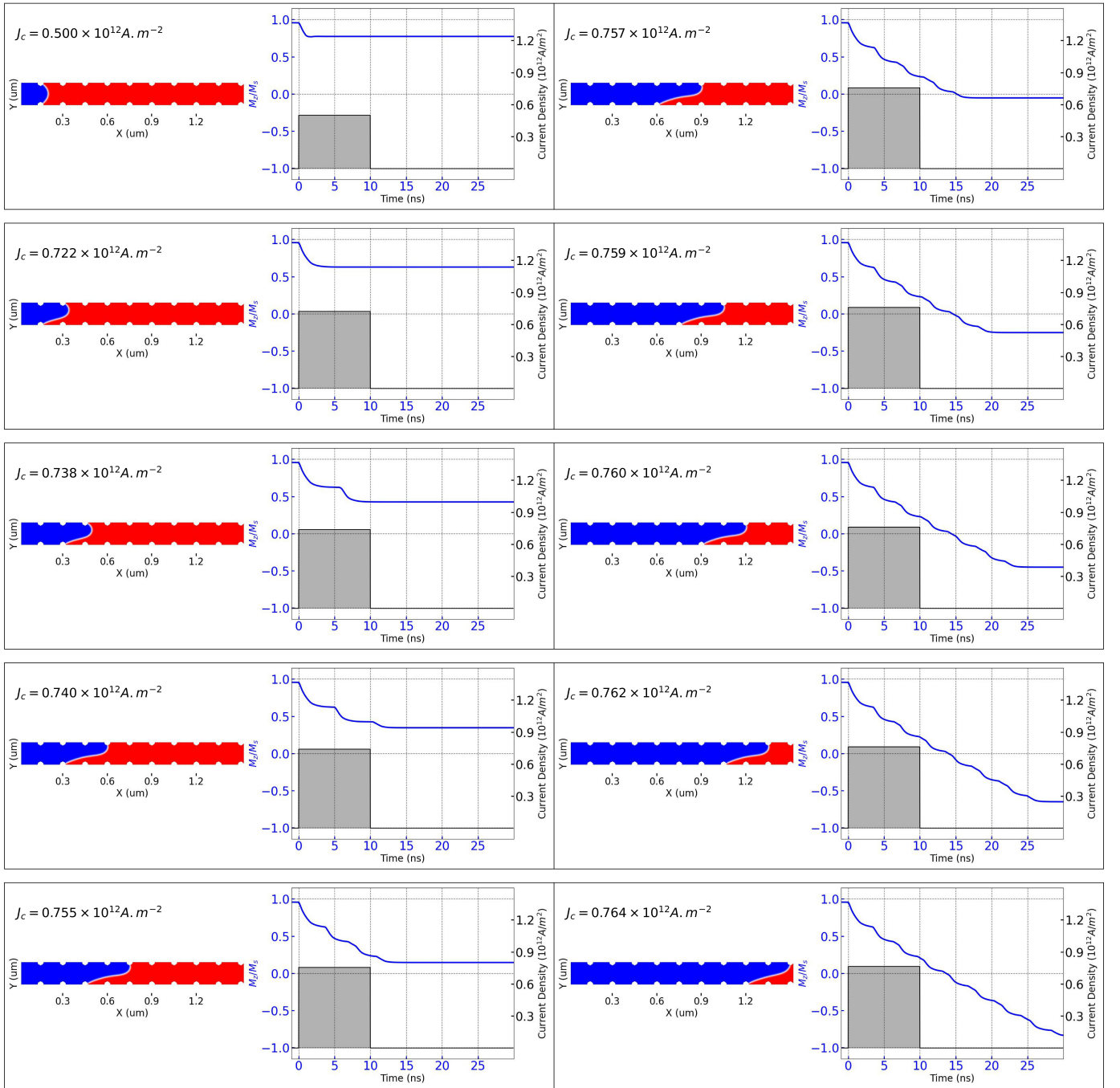


FIG. 3. **Domain wall dynamics through the corrugated magnetic nanotrack with 10 symmetrical notches.** The magnetization profile within the corrugated magnetic notches as a function of increasing current density of the 10 ns current pulse are shown in left and the corresponding magnetization dynamics are shown in right at different current densities, the black-shaded region depicts the 10 ns current pulse with increasing current density in each case. The step-like behaviour suggests the pinning of the domain wall at the engineered equidistant notches on the magnetic nanotrack.

the required current density, which translates to a reduced domain wall velocity of  $\sim 75$  m/s. Thus, the DW motion has been engineered by placing the notches in the desired locations. Similar magnetization profile and time-resolved magnetization dynamics has also been shown for a nanotrack containing 10 symmetrical notches in Fig. 3. The pinning of the domain wall at the first notch in the 10-notch system starts at the same current density ( $J_c = 0.500 \times 10^{12}$  A.m $^{-2}$ )

as for 5-notch system. However, it takes considerable lesser current ( $J_c = 0.764 \times 10^{12}$  A.m $^{-2}$ ) to fully switch the 10-notch system.

In the magnetic nanotrack with equally spaced, identical notches, each notch serves as a pinning centre by creating a localized energy barrier[44]. For the DW to move past a notch, its energy, driven by current, must overcome this barrier. The event of depinning, as well as the movement

of the DW under an applied current, involves energy dissipation through magnetic damping. As a result, the effective potential barrier is increased for each successive notch, requiring larger current densities to overcome the pinning sites. Additionally, the DW accumulates elastic strain while pinned, which helps it de-pin and settle at the next site as the current increases. Each depinning event reconfigures the DWs chiral structure corresponding energy, making it more susceptible to pinning at the following notch. Notably, the magnetization decay is featured with a step-like pattern, indicating temporary halts of the DW motion at each pinning site. The step-like displacement and selective pinning of the DW in response to the current closely parallels neuromorphic computing, mimicking the gradual and quantized changes of synaptic weights in biological synapses. Each pinning site acts as a meta state, allowing incremental adjustments equivalent to synaptic weight updates. This controlled, stepwise depinning is also ideal for implementing gradual learning, where DWs held at notches retain memory until a higher current prompts movement-similar to the plasticity and non-volatile nature of synaptic weights that maintain information without constant power.

Without notch-type corrugations, the DW movements nearly linear, controlled both by the applied current density and DMI energy, which determines the DW velocity. The corrugations provide us another knob to control the DW movements and enable lithographic control of synaptic weight values. Other methods for DW pinning include using interlayer exchange coupling of multiple MTJs or by introducing defects in the shape or anisotropy of the FL. However, notches were chosen as the preferred pinning method because their controllable positions guarantee update linearity, which cannot readily be obtained using randomly distributed defects. In addition, notches are less complex to lithographically define than interlayer exchange and can be more easily scaled. Similar to the neuron conductance detector, the DW position is converted to a synapse conductance using a typical MTJ structure, with a parallel resistance of 10 k $\Omega$  and antiparallel resistance of 20 k $\Omega$ . Depending on the position of the DW, the resistance changes linearly based on the magnetization of the FL.

#### IV. NEURAL NETWORK INTEGRATION

In this section, we describe how our proposed devices can be utilized to build a fully-connected ANN. We train a neural network using two benchmark datasets, MNIST handwritten digit dataset and Fashion MNIST dataset. Both datasets contain 60000 training and 10000 test grayscale images with a size of 28 $\times$ 28 pixels. Here, we use a three-layer fully connected neural network with 784 nodes for the input layer, 128 nodes for the hidden layer, and 10 nodes for the output layer. A schematic of the neural network is shown in Fig. 4(a) and 5(a) for the MNIST handwritten digit dataset and the Fashion MNIST dataset, respectively. The activation function of the neurons is implemented using the ReLU-like behavior that is obtained from our proposed neuron device (Fig. 1(b)).

First, we train the fully connected neural network using PyTorch, a package used to build and train machine learning

models, where we utilize the default float32 (FP32) weights for the model. A distribution of the trained weights for the input to the hidden layer is shown in Fig. 4(c) and Fig. 5(c) for the MNIST digit dataset and the Fashion MNIST dataset, respectively. The simulation results show a test accuracy of  $\sim$ 97% for the MNIST and  $\sim$ 86% for the Fashion MNIST dataset. The detailed test accuracy for different variants of our proposed synaptic device is provided in the Table II, that shows a negligible variation between these different variants for any particular dataset.

TABLE II. Result Summary for the test accuracy (in %)

Conductance Levels	Dataset	FP32	Quantized	Fine Tune
10-notch system	MNIST	97.41	94.67	97.17
	FashionMNIST	86.40	62.20	86.22
5-notch system	MNIST	97.41	93.84	96.91
	FashionMNIST	86.40	61.36	86.31

Key difference between the test accuracies is seen for MNIST and Fashion MNIST datasets, which arises due to the complex nature of the Fashion MNIST dataset with respect to the MNIST one. This difference can be understood in depth with the help of confusion matrix, as shown in Fig. 4(d) and Fig. 5(d), for the MNIST and Fashion MNIST datasets, respectively. As the MNIST images are quite distinct from each other, so there is a slight mismatch among the actual and predicted label. On the other hand, Fashion MNIST dataset contains many similar looking ambiguous images with different actual labels, leading to wrong prediction. For example, a key ambiguity comes from the images with labels like ‘Shirt’, ‘T-shirt/top’, ‘Pullover’, which is clearly visible from the number of wrong predictions in confusion matrix of Fig 5(d), leading to relatively lower test accuracy for the Fashion MNIST dataset.

As an example, a few misinterpreted results of the Fashion MNIST dataset for the FP32 weights are shown in Fig.6, which clearly demonstrates the ambiguous nature of the test images. To incorporate the effects of distinct synaptic weights of our proposed devices, we quantize the trained FP32 weights into discrete normalized conductance values/levels, mirroring the synaptic states of the DW-based synapse device. The distribution of purely quantized synaptic weights connecting input and hidden layer for MNIST and Fashion MNIST dataset are shown in Fig. 4(e) and Fig. 5(e), respectively for the 10 notch device. A similar quantization can also be done with the conductance states obtained from 5 notch devices, which we do not show here. From these figures, we notice that the weights are very sparse and only present at the given synaptic weight levels. The corresponding test accuracy for the MNIST dataset is  $\sim$ 94%, however a drastic change is noticeable for the Fashion MNIST dataset, where the test accuracy is  $\sim$ 62%. The degradation of the test accuracy is due to synaptic weight distribution at purely quantized levels, instead of entire weight range. The degradation in the test accuracy can also be visible by comparing the confusion matrix of Fig. 4(d) and (f), corresponding to FP32 and pure quantized weights. Lower values of the diagonal elements of the confusion matrix corresponding to pure quantized weights (Fig. 4(f)) compared to FP32 weights (Fig. 4(d)) reflects this degradation. The drastic change corresponding to the Fashion MNIST dataset is due to the

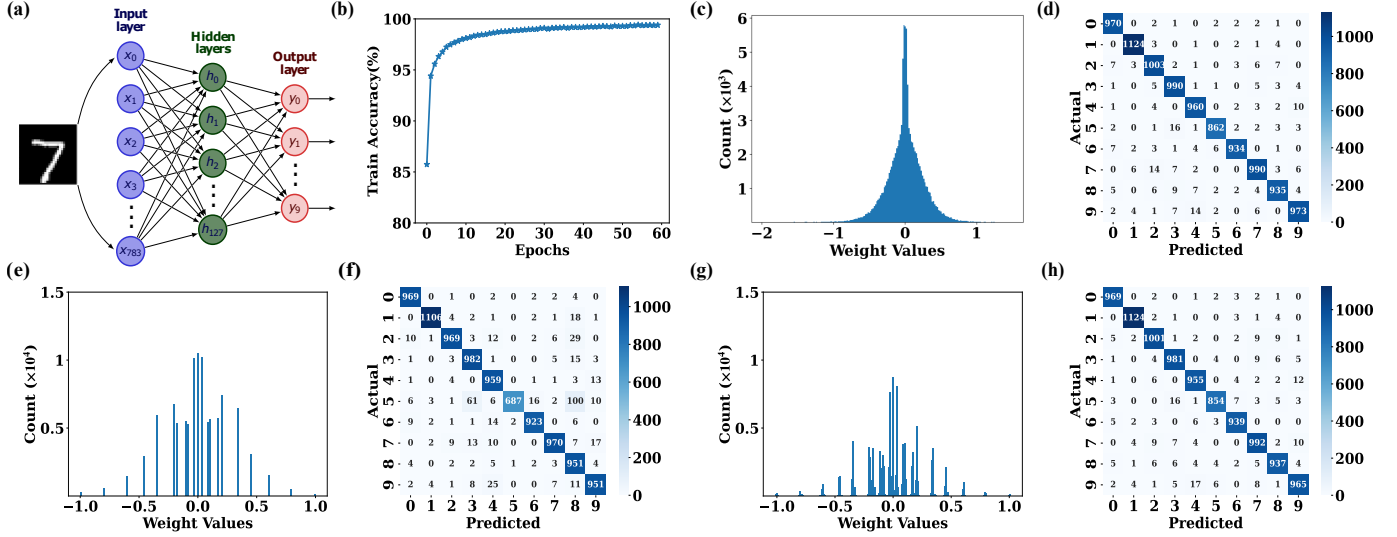


FIG. 4. (a) Schematic of fully connected Neural Network for identifying MNIST dataset images, (b) plot of Training accuracy with epochs for FP32 weights, (c) FP32 synaptic Weight distribution from input to hidden layer, (d) Confusion Matrix for FP32 synaptic weights, (e) Synaptic weight distribution of input to hidden layer for pure quantized weights, (f) Confusion Matrix of pure quantized synaptic weights, (g) Synaptic weight distribution for the input to hidden layer fine tuning of the synaptic weights, (h) Confusion Matrix for the fine tuned synaptic weights.

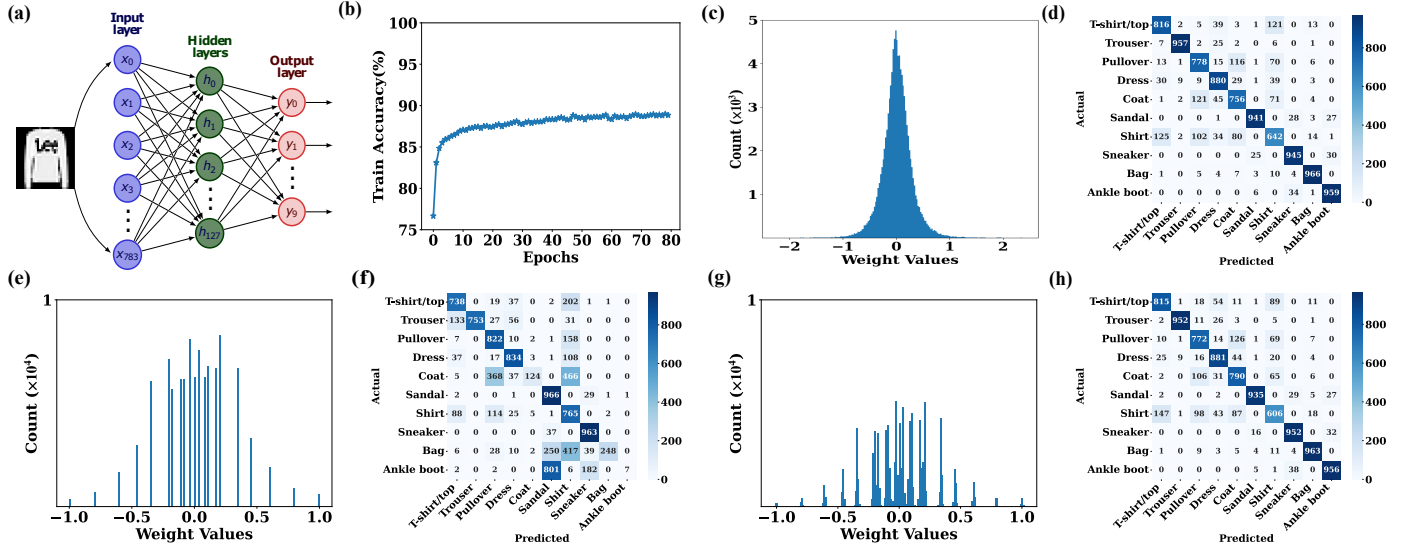


FIG. 5. (a) Schematic of fully connected Neural Network for identifying Fashion MNIST dataset images, (b) plot of Training accuracy with epochs for FP32 weights, (c) FP32 synaptic Weight distribution from input to hidden layer, (d) Confusion Matrix for FP32 synaptic weights, (e) Synaptic weight distribution of input to hidden layer for pure quantized weights, (f) Confusion Matrix of pure quantized synaptic weights, (g) Synaptic weight distribution for the input to hidden layer fine tuning of the synaptic weights, (h) Confusion Matrix for the fine tuned synaptic weights.

complex and ambiguous nature of the images as discussed earlier. Due to the ambiguity among inter-class images, there are a noticeable mismatch in the off-diagonal elements of the confusion matrix in Fig. 5(f). For the fine-tuning, we retrain the model with pure quantized weights. The weight distribution of the fine-tuned model, are shown in Fig. 4(g) and Fig. 5(g) for MNIST and Fashion MNIST dataset. This shows a narrow distribution around the discrete quantized labels. Such distributions can naturally occur

in synaptic weights derived from experimentally fabricated devices, where inherent conductance variations typically fluctuate around a mean value. Table II shows that the fine-tuned model improves the accuracy and the test accuracy becomes similar to the FP32 weights. Comparison of the confusion matrix between the fine-tuned model and the pure quantized model reflects the improvement of the test accuracy. The complete results for the 5-notch and 10-notch systems are summarized in Table II. These data

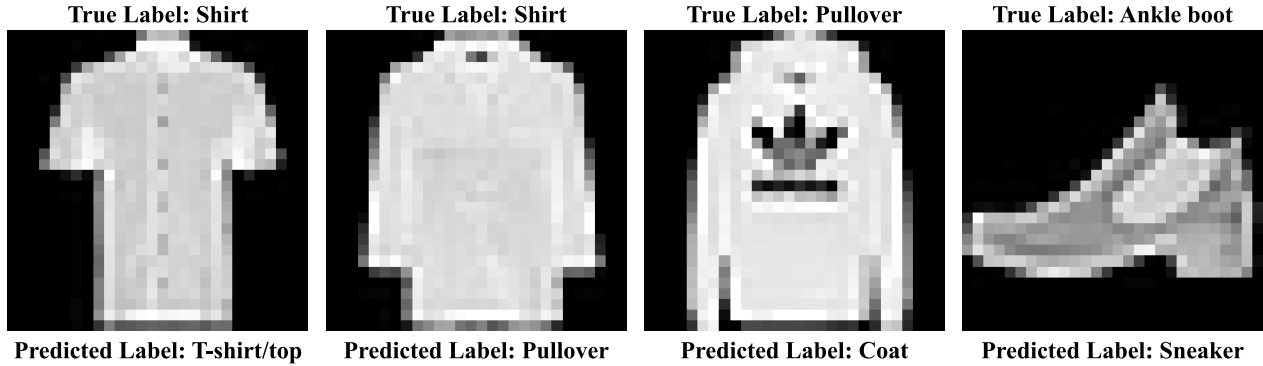


FIG. 6. Misinterpreted results of the Fashion MNIST dataset for FP32 weights.

demonstrate that while the system initially suffers from a degradation in test accuracy, subsequent fine-tuning effectively recovers the performance, bringing the accuracy closer to its baseline (FP32) value.

## V. CONCLUSIONS

We have presented a robust framework for simulating and implementing a fully connected ANN utilizing SOT-driven spintronic devices. Using transverse DW dynamics in HM/FM nanotrack, we have successfully emulated the critical functionalities of both artificial neurons and synapses. Our approach bridges the gap between fundamental DW driven magnetization switching and neuromorphic computing architectures, offering a viable pathway toward highly efficient, brain-inspired computational hardware. At the device level, our micromagnetic simulations establish that the ReLU activation function of a neuron can be accurately mimicked through DW motion triggered by a 3 ns current pulse in a HM/FM nanotrack. More critically, we engineered the synaptic behavior by introducing semicircular notch-type corrugations, symmetrically located along another HM/FM nanotrack. Under the influence of 10 ns current pulse with varying current densities, these geometric constraints effectively serve as discrete pinning sites for the domain

wall. This configuration results in a highly controlled, step-like DW motion characterized by temporary pauses at each pinning center. We have demonstrated that the electrical conductance of the DW at these specific pinned locations provides stable, distinct states that seamlessly translate into programmable synaptic weights for the ANN. Furthermore, our investigation revealed a crucial threshold-dependent delay effect during the depinning process. Because each depinning event is intrinsically influenced by the history of previous states, the device inherently mirrors the synaptic memory, plasticity, and temporal adaptability found in biological neural systems. To validate the system-level performance of our proposed neuro-synaptic devices, we evaluated the fully connected ANN using standard FP32 synaptic weights. Testing on the benchmark MNIST and Fashion-MNIST datasets yielded impressive classification accuracies of approximately  $\sim 97\%$  and  $\sim 86\%$ , respectively. These baseline results confirm that the physical dynamics of DW pinning and depinning can be reliably mapped to complex algorithmic requirements without a fundamental loss of computational fidelity. Ultimately, this work underscores the immense potential of domain wall dynamics in constrained geometries for the future of adaptive computation.

## REFERENCES

- 
- \* [debanjan.polley@hyderabad.bits-pilani.ac.in](mailto:debanjan.polley@hyderabad.bits-pilani.ac.in)
- [1] W. S. McCulloch and W. Pitts, "A logical calculus of the ideas immanent in nervous activity," *The bulletin of mathematical biophysics*, vol. 5, no. 4, pp. 115–133, 1943.
  - [2] D. O. Hebb, *The organization of behavior: A neuropsychological theory*. 1949.
  - [3] D. Li, X. Chen, M. Becchi, and Z. Zong, "Evaluating the energy efficiency of deep convolutional neural networks on cpus and gpus," in *2016 IEEE international conferences on big data and cloud computing (BDCloud), social computing and networking (SocialCom), sustainable computing and communications (SustainCom)(BDCloud-SocialCom-SustainCom)*, pp. 477–484, IEEE, 2016.
  - [4] Y. Hong, B. Hou, H. Jiang, and J. Zhang, "Machine learning and artificial neural network accelerated computational discoveries in materials science," *Wiley Interdisciplinary Reviews: Computational Molecular Science*, vol. 10, no. 3, p. e1450, 2020.
  - [5] J. Lee, A. Seko, K. Shitara, K. Nakayama, and I. Tanaka, "Prediction model of band gap for inorganic compounds by combination of density functional theory calculations and machine learning techniques," *Physical Review B*, vol. 93, no. 11, p. 115104, 2016.
  - [6] A. Tarbi, T. Chtouki, Y. Elkouari, H. Erguig, A. Migalska-Zalas, and A. Aissat, "Bandgap energy modeling of the deformed ternary  $\text{GaAs}_{1-x}\text{In}_x$  by artificial neural networks," *Heliyon*, vol. 8, no. 8, 2022.
  - [7] S. Agatonovic-Kustrin and R. Beresford, "Basic concepts of artificial neural network (ann) modeling and its application in pharmaceutical research," *Journal of pharmaceutical and*

- biomedical analysis*, vol. 22, no. 5, pp. 717–727, 2000.
- [8] I. I. Baskin, D. Winkler, and I. V. Tetko, “A renaissance of neural networks in drug discovery,” *Expert opinion on drug discovery*, vol. 11, no. 8, pp. 785–795, 2016.
  - [9] A. Krizhevsky, I. Sutskever, and G. E. Hinton, “Imagenet classification with deep convolutional neural networks,” *Advances in neural information processing systems*, vol. 25, 2012.
  - [10] K. Gopalakrishnan, S. K. Khaitan, A. Choudhary, and A. Agrawal, “Deep convolutional neural networks with transfer learning for computer vision-based data-driven pavement distress detection,” *Construction and building materials*, vol. 157, pp. 322–330, 2017.
  - [11] M. Xiao, Y. Li, X. Yan, M. Gao, and W. Wang, “Convolutional neural network classification of cancer cytopathology images: taking breast cancer as an example,” in *Proceedings of the 2024 7th International Conference on Machine Vision and Applications*, pp. 145–149, 2024.
  - [12] Y. Pan, W. Huang, Z. Lin, W. Zhu, J. Zhou, J. Wong, and Z. Ding, “Brain tumor grading based on neural networks and convolutional neural networks,” in *2015 37th annual international conference of the IEEE engineering in medicine and biology society (EMBC)*, pp. 699–702, IEEE, 2015.
  - [13] S. Yu, “Neuro-inspired computing with emerging nonvolatile memories,” *Proceedings of the IEEE*, vol. 106, no. 2, pp. 260–285, 2018.
  - [14] S. Yu, W. Shim, X. Peng, and Y. Luo, “Rram for compute-in-memory: From inference to training,” *IEEE Transactions on Circuits and Systems I: Regular Papers*, vol. 68, no. 7, pp. 2753–2765, 2021.
  - [15] A. Baroni, A. Glukhov, E. Perez, C. Wenger, D. Ielmini, P. Olivo, and C. Zambelli, “Low conductance state drift characterization and mitigation in resistive switching memories (rram) for artificial neural networks,” *IEEE Transactions on Device and Materials Reliability*, vol. 22, no. 3, pp. 340–347, 2022.
  - [16] G. W. Burr, R. M. Shelby, S. Sidler, C. Di Nolfo, J. Jang, I. Boybat, R. S. Shenoy, P. Narayanan, K. Virwani, E. U. Giacometti, *et al.*, “Experimental demonstration and tolerancing of a large-scale neural network (165 000 synapses) using phase-change memory as the synaptic weight element,” *IEEE Transactions on Electron Devices*, vol. 62, no. 11, pp. 3498–3507, 2015.
  - [17] G. W. Burr, M. J. Brightsky, A. Sebastian, H.-Y. Cheng, J.-Y. Wu, S. Kim, N. E. Sosa, N. Papandreou, H.-L. Lung, H. Pozidis, *et al.*, “Recent progress in phase-change memory technology,” *IEEE Journal on Emerging and Selected Topics in Circuits and Systems*, vol. 6, no. 2, pp. 146–162, 2016.
  - [18] A. Sebastian, M. Le Gallo, and E. Eleftheriou, “Computational phase-change memory: Beyond von neumann computing,” *Journal of Physics D: Applied Physics*, vol. 52, no. 44, p. 443002, 2019.
  - [19] L. Wang, G. Ma, S. Yan, X. Cheng, and X. Miao, “Reconfigurable multilevel storage and neuromorphic computing based on multilayer phase-change memory,” *ACS Applied Materials & Interfaces*, vol. 16, no. 40, pp. 54829–54836, 2024.
  - [20] A. Sengupta, Y. Shim, and K. Roy, “Proposal for an all-spin artificial neural network: Emulating neural and synaptic functionalities through domain wall motion in ferromagnets,” *IEEE transactions on biomedical circuits and systems*, vol. 10, no. 6, pp. 1152–1160, 2016.
  - [21] A. Ross, N. Leroux, A. De Riz, D. Marković, D. Sanz-Hernández, J. Trastoy, P. Bortolotti, D. Querlioz, L. Martins, L. Benetti, *et al.*, “Multilayer spintronic neural networks with radiofrequency connections,” *Nature Nanotechnology*, vol. 18, no. 11, pp. 1273–1280, 2023.
  - [22] B. Chen, M. Zeng, K. H. Khoo, D. Das, X. Fong, S. Fukami, S. Li, W. Zhao, S. S. Parkin, S. Piramanayagam, *et al.*, “Spintronic devices for high-density memory and neuromorphic computing—a review,” *Materials Today*, vol. 70, pp. 193–217, 2023.
  - [23] A. Kumar, D. Das, D. J. Lin, L. Huang, S. L. Yap, H. K. Tan, R. J. Lim, H. R. Tan, Y. T. Toh, S. Ter Lim, *et al.*, “Bimodal alteration of cognitive accuracy for spintronic artificial neural networks,” *Nanoscale Horizons*, vol. 9, no. 9, pp. 1522–1531, 2024.
  - [24] T. Seifert, S. Jaiswal, U. Martens, J. Hannegan, L. Braun, P. Maldonado, F. Freimuth, A. Kronenberg, J. Henrizi, I. Radu, *et al.*, “Efficient metallic spintronic emitters of ultrabroadband terahertz radiation,” *Nature photonics*, vol. 10, no. 7, pp. 483–488, 2016.
  - [25] D. Polley, A. Pattabi, A. Rastogi, K. Jhuria, E. Diaz, H. Singh, A. Lemaitre, M. Hehn, J. Gorchon, and J. Bokor, “Picosecond spin-orbit torque-induced coherent magnetization switching in a ferromagnet,” *Science Advances*, vol. 9, no. 36, p. eadh5562, 2023.
  - [26] D. Polley, A. Pattabi, J. Chatterjee, S. Mondal, K. Jhuria, H. Singh, J. Gorchon, and J. Bokor, “Progress toward picosecond on-chip magnetic memory,” *Applied Physics Letters*, vol. 120, no. 14, 2022.
  - [27] D. Fan, Y. Shim, A. Raghunathan, and K. Roy, “Stt-snn: A spin-transfer-torque based soft-limiting non-linear neuron for low-power artificial neural networks,” *IEEE Transactions on Nanotechnology*, vol. 14, no. 6, pp. 1013–1023, 2015.
  - [28] Y. Zhang, W. Zhao, J.-O. Klein, W. Kang, D. Querlioz, Y. Zhang, D. Ravelosona, and C. Chappert, “Spintronics for low-power computing,” in *2014 Design, Automation & Test in Europe Conference & Exhibition (DATE)*, pp. 1–6, IEEE, 2014.
  - [29] G. Finocchio, M. Di Ventra, K. Y. Camsari, K. Everschor-Sitte, P. K. Amiri, and Z. Zeng, “The promise of spintronics for unconventional computing,” *Journal of Magnetism and Magnetic Materials*, vol. 521, p. 167506, 2021.
  - [30] X. Fong, Y. Kim, K. Yogendra, D. Fan, A. Sengupta, A. Raghunathan, and K. Roy, “Spin-transfer torque devices for logic and memory: Prospects and perspectives,” *IEEE Transactions on Computer-Aided Design of Integrated Circuits and Systems*, vol. 35, no. 1, pp. 1–22, 2015.
  - [31] S. Mondal, D. Polley, A. Pattabi, J. Chatterjee, D. Salomoni, L. Aviles-Felix, A. Olivier, M. Rubio-Roy, B. DiÁny, L. D. B. Prejbeanu, R. Sousa, I. L. Prejbeanu, and J. Bokor, “Single-shot switching in tb/co-multilayer based nanoscale magnetic tunnel junctions,” *Journal of Magnetism and Magnetic Materials*, vol. 581, p. 170960, 2023.
  - [32] S. S. Parkin, C. Kaiser, A. Panchula, P. M. Rice, B. Hughes, M. Samant, and S.-H. Yang, “Giant tunnelling magnetoresistance at room temperature with mgo (100) tunnel barriers,” *Nature materials*, vol. 3, no. 12, pp. 862–867, 2004.
  - [33] X. Fong, S. H. Choday, and K. Roy, “Bit-cell level optimization for non-volatile memories using magnetic tunnel junctions and spin-transfer torque switching,” *IEEE Transactions on Nanotechnology*, vol. 11, no. 1, pp. 172–181, 2011.
  - [34] Z. He, S. Angizi, and D. Fan, “Exploring stt-mram based in-memory computing paradigm with application of image edge extraction,” in *2017 IEEE International Conference on Computer Design (ICCD)*, pp. 439–446, IEEE, 2017.
  - [35] C. Wang, D. Zhang, L. Zeng, E. Deng, J. Chen, and W. Zhao, “A novel mtj-based non-volatile ternary content-addressable memory for high-speed, low-power, and high-reliable search operation,” *IEEE Transactions on Circuits and Systems I: Regular Papers*, vol. 66, no. 4, pp. 1454–1464, 2018.

- [36] C. Cui, O. G. Akinola, N. Hassan, C. H. Bennett, M. J. Marinella, J. S. Friedman, and J. A. C. Incorvia, "Maximized lateral inhibition in paired magnetic domain wall racetracks for neuromorphic computing," *Nanotechnology*, vol. 31, no. 29, p. 294001, 2020.
- [37] T. Szandała, "Review and comparison of commonly used activation functions for deep neural networks," in *Bio-inspired neurocomputing*, pp. 203–224, Springer, 2020.
- [38] D. Das, Y. Cen, J. Wang, and X. Fong, "Bilayer-skyrmion-based design of neuron and synapse for spiking neural network," *Physical Review Applied*, vol. 19, no. 2, p. 024063, 2023.
- [39] M. J. Donahue and D. G. Porter, "OOMMF user's guide, version 2.0a0," 2019. <http://math.nist.gov/oommf/>.
- [40] S. Rohart and A. Thiaville, "DMExchange6Ngbr: OOMMF oxs extension modules," 2012. <https://math.nist.gov/oommf/contrib/oxsext>.
- [41] M. Beg, M. Lang, and H. Fangohr, "Ubermag: Toward more effective micromagnetic workflows," *IEEE Transactions on Magnetics*, vol. 58, no. 2, pp. 1–5, 2021.
- [42] Y. Huang, W. Kang, X. Zhang, Y. Zhou, and W. Zhao, "Magnetic skyrmion-based synaptic devices," *Nanotechnology*, vol. 28, no. 8, p. 08LT02, 2017.
- [43] R. V. Ababei, M. O. Ellis, I. T. Vidamour, D. S. Devadasan, D. A. Allwood, E. Vasilaki, and T. J. Hayward, "Neuromorphic computation with a single magnetic domain wall," *Scientific Reports*, vol. 11, no. 1, p. 15587, 2021.
- [44] S. J. Noh, Y. Miyamoto, M. Okuda, N. Hayashi, and Y. Keun Kim, "Effects of notch shape on the magnetic domain wall motion in nanowires with in-plane or perpendicular magnetic anisotropy," *Journal of Applied Physics*, vol. 111, no. 7, 2012.